Supporting Information (SI) *for*:

In-situ Topology Synthesis of Orthorhombic NaV_2O_5 with High Pseudocapacitive Contribution for Lithium-ion Battery Anode

*Wenbin Li,[a] Jianfeng Huang,[*a] Liyun Cao,[a] Yijun Liu,[b] Limin Pan,[b] Liangliang Feng,[*a]*

[a] School of Materials Science & Engineering, Shaanxi University of Science and Technology, Weiyang university campus, Xi'an Shaanxi 710021, P.R. China.
[b] Monalisa Group CO.,LTD, Taiping industrial zone, xiqiao town, nanhai district, Foshan,Guangdong 528200, P.R. China.

E-mail: huangjf@sust.edu.cn, fengll@sust.edu.cn

Number of pages: 13

Number of figures: 11

Number of tables: 1

Experimental work

Material synthesis

All these starting materials were of analytical grade and directly used without further purifications. 1.0 g $NaVO_3$ (Aladdin) and 0.08 g $Na_2S{\cdot}9H_2O$ (Sinopharm Chemical Reagent) were first dissolved in 60 ml of deionized (DI) water assisted by magnetic stirring at room temperature. The reaction solution was then transferred to a 100 mL Teflon-lined stainless steel autoclave, and heated at 200 °C for 24 h at a rotating speed of 10 rpm. After it naturally cooled back to room temperature, the solid precipitate in the autoclave was collected by filtration, washed with DI water and ethanol in turn for three times, and dried in a vacuum oven at 60 ^{o}C for 12 h. The raw $NaVO_3$ and the as-synthesized NaV_2O_5 are abbreviated as *m*-$NaVO_3$ and *o*-NaV_2O_5, respectively.

Materials characterization

Powder XRD patterns were obtained using a D/max2200PC X-ray diffractometer with Cu Ka X-ray source (λ=0.15406 nm)) at room temperature. Raman spectra were taken on a Renishaw-invia confocal microprobe Raman system. Infrared spectra were obtained on a VECTOR-22 Bruker Alpha type infrared spectrometer. XPS spectra were collected on AXIS SUPRA X-ray photoelectron spectrometer (XPS) with monochromatic Al Kα radiation as the X-ray source. SEM (scanning electron microscope) images were taken on an S-4800 field emission scanning electron microscope. TEM (transmission electron microscopy) was carried out on a JEM-3010 high-resolution transmission electron microscopy. ICP-AES (Inductively Coupled

Plasma-Atomic Emission Spectrometry) elemental analysis was performed on an IRIS Intrepid 2 ICP spectrometer.

Electrochemical test

The slurry was fabricated by mixing the as-synthesized electrode materials, acetylene black and polyvinylidene fluoride (PVDF) binder in a weight ratio of 80:10:10 using N-methyl-2-pyrrolidone (NMP) as solution. To prepare working electrodes, the slurry was blade-coated onto a Cu foil, and vacuum-dried at 60 °C for 12 h. The diameter of electrode roundel was 16 mm and the areal loading of active material was 0.8 ~ 1.2 mg/cm^2. The working electrodes were assembled into CR2032-type button cells in an Ar-filled glove box by pairing the working electrode with a piece of Li foil. The separator was a microporous polypropylene film. The electrolyte was a solution containing 1 M $LiPF_6$ in a mixture of ethylene carbonate, ethyl methyl carbonate, and DMC (1:1:1 in volume). Galvanostatic charge and discharge experiments at different current densities were carried out on a CT2001A LANHE battery testing system at a potential range of 0.01 ~ 3.00 V *vs*. Li^+/Li . Cyclic voltammetry (CV) and electrochemical impedance spectroscopy (EIS) measurements were carried out using a CHI660E electrochemical workstation. All of the measurements were carried out at room temperature [1-2].

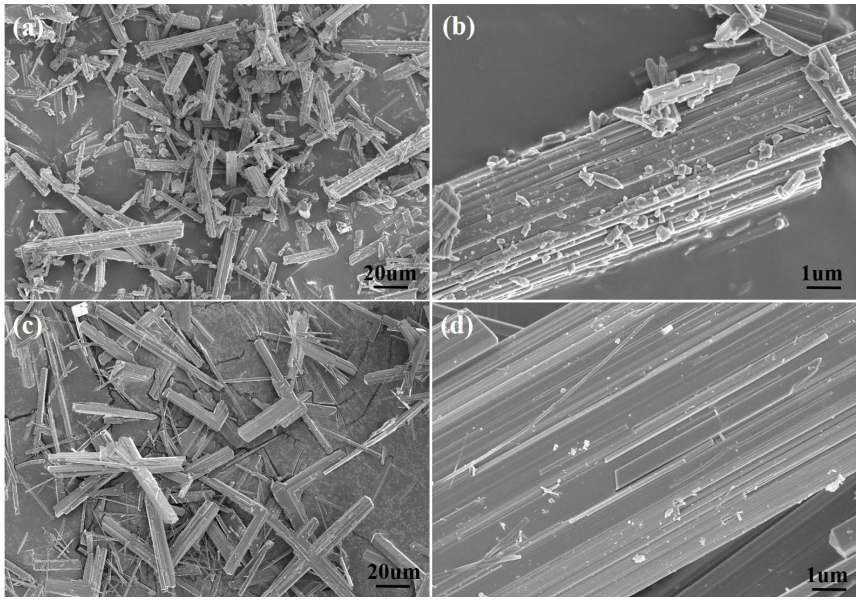

Figure S1. SEM images of (a, b) *m*-$NaVO_3$ and (c, d) *o*-NaV_2O_5.

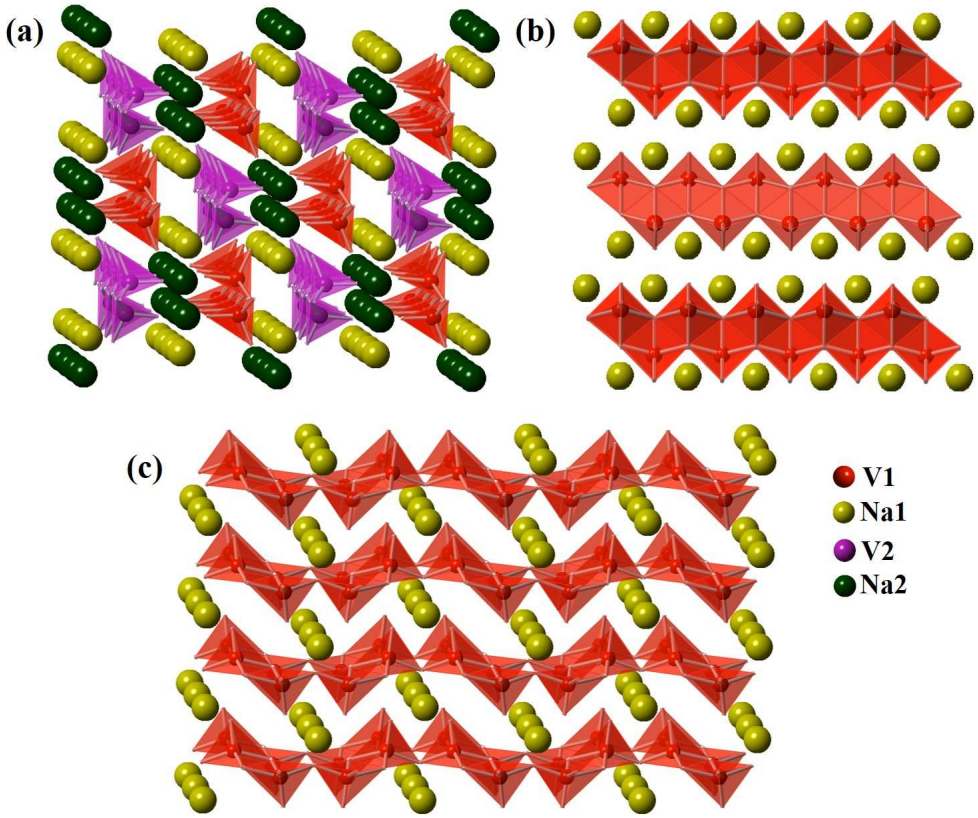

Figure S2. Crystal structure model of (a) Monoclinic $NaVO_3$, (b) Orthorhombic $NaVO_3$ and (c) Orthorhombic NaV_2O_5.

Table S1 Raman frequencies and corresponding vibration modes of *o*-NaV_2O_5.

Observed Raman frequency	Vibration mode
141	Na ∥ *a*
171	Na ∥ *c*
234	V-O-V bending
257	V-O-V bending
296	V-O-V bending
419	V-O-V bending
484	V-O3-V bending
528	V-O2 stretching
968	V=O1 stretching

Particularly, a strong peak at 171 cm^{-1} is originated from the displacement of fully ionized Na-ions along the *c* axis, and a weak band at 141 cm^{-1} is ascribed to the rotation of $(V_2O_4)_n$ chains along the *a* axis.

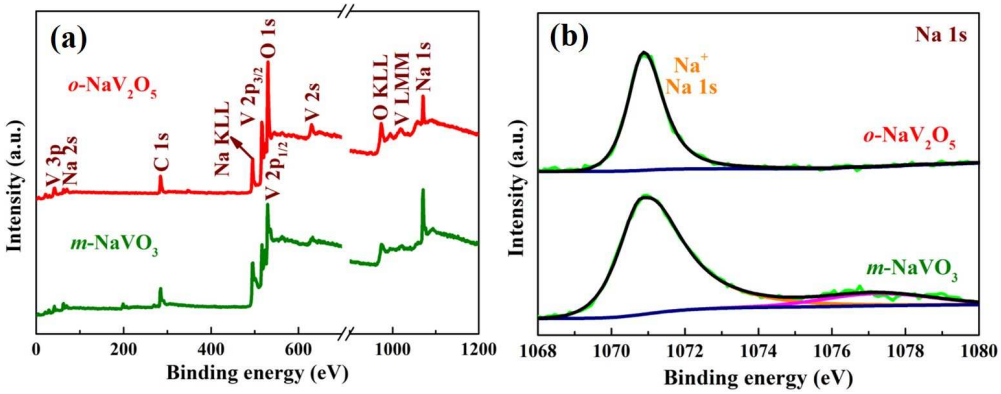

Figure S3. (a) Survey XPS spectra and (b) High-resolution Na 1s XPS spectra of *m*-$NaVO_3$ and *o*-NaV_2O_5.

In the survey XPS spectra (Figure S3(a)), the molar ratio of Na/V is calculated to be ~ 1:1 for *m*-$NaVO_3$ and ~ 1:2 for *o*-NaV_2O_5.

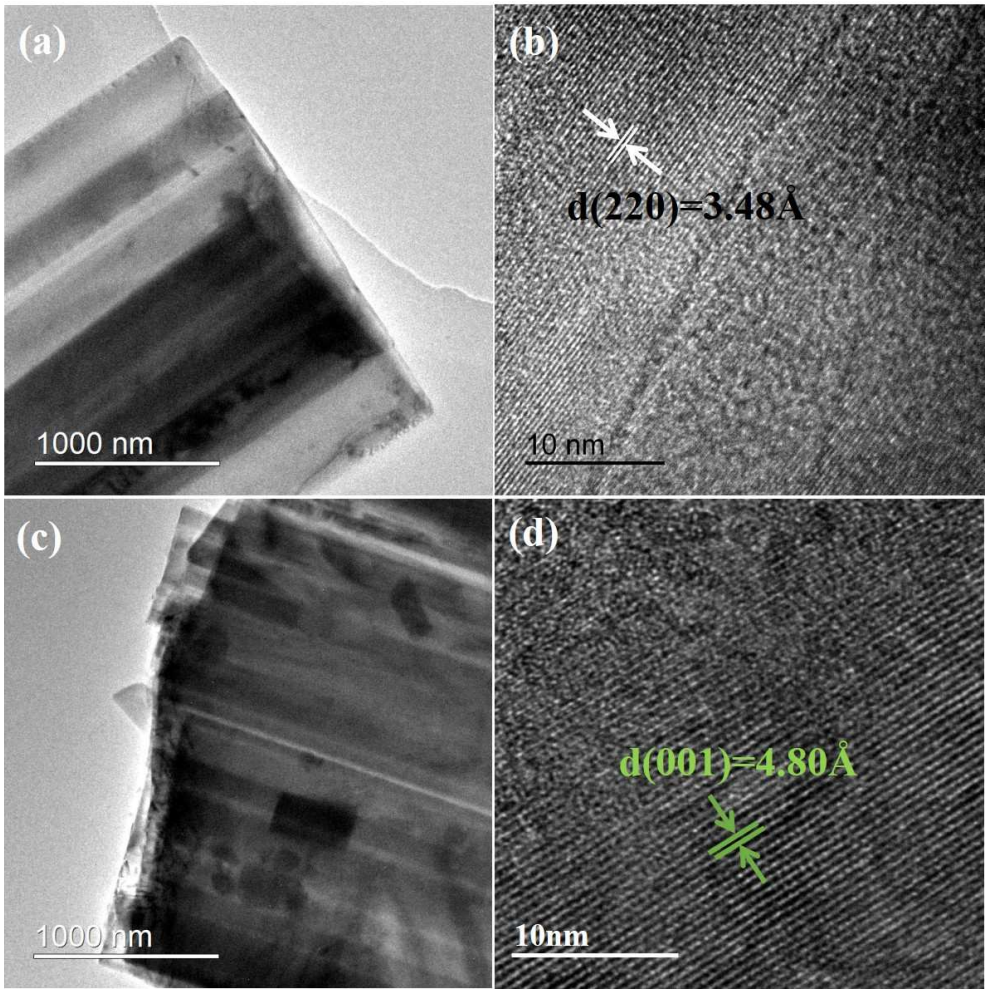

Figure S4. TEM images of (a) *m*-$NaVO_3$ and (c) *o*-NaV_2O_5, and HRTEM images of (b) *m*-$NaVO_3$ and (d) *o*-NaV_2O_5.

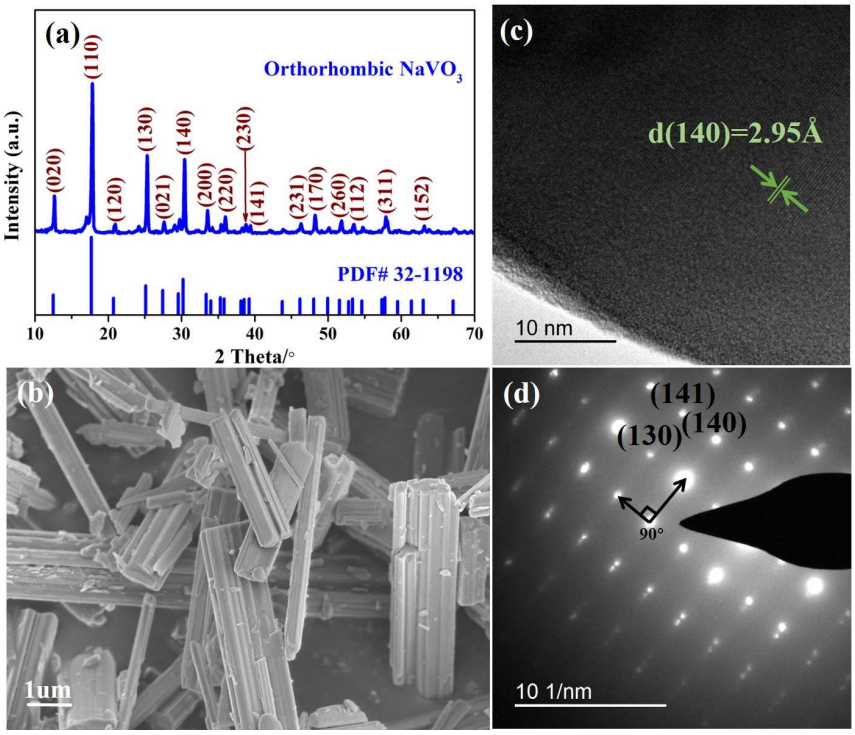

Figure S5. (a) XRD pattern, (b) SEM image, (c) HRTEM image and (d) SAED image of orthorhombic $NaVO_3$.

$$12VO_3^- + S^{2-} + 3H_2O \rightarrow 6V_2O_5^- + SO_3^{2-} + 6OH^- \quad \text{(S1)}$$

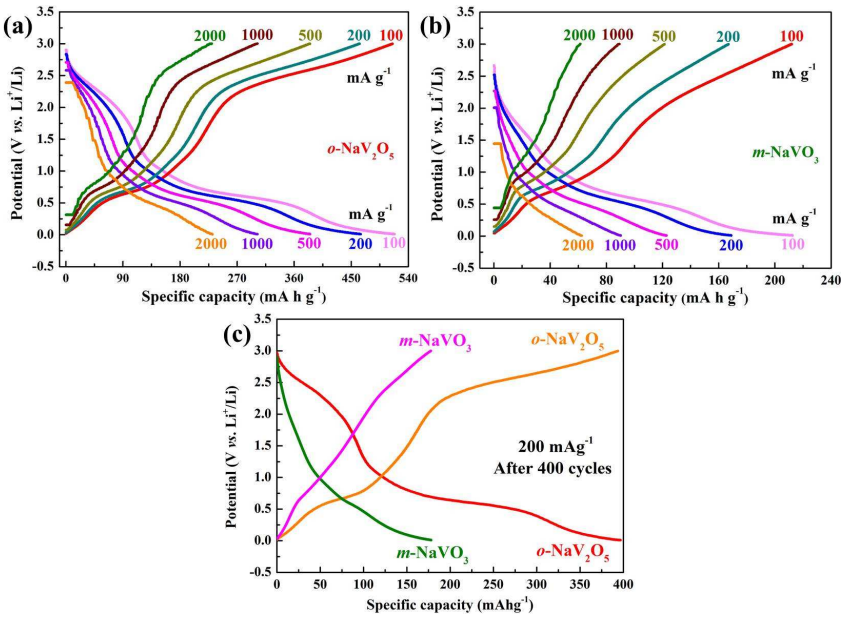

Figure S6. Charge/discharge profiles of (a) *o*-NaV_2O_5 and (b) *m*-$NaVO_3$ electrode at various current densities from 100 to 2000 mAg^{-1}.Charge/discharge profiles of *o*-NaV_2O_5 and *m*-$NaVO_3$ electrode after 400 cycles.

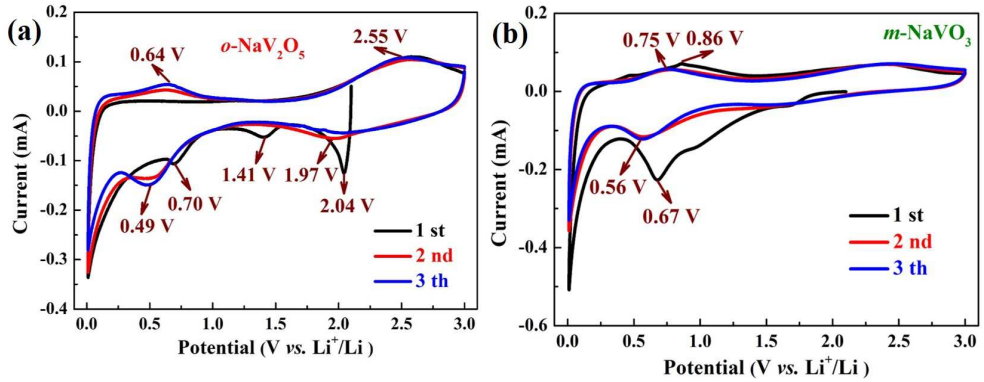

Figure S7. First three CV curves at a scan rate of 0.1 mVs^{-1} for (a) *o*-NaV_2O_5 and (b) *m*-$NaVO_3$ electrode.

As shown in Figure S7, two weak peaks at ~1.41 and 0.70 V for *o*-NaV_2O_5 electrode and a strong peak at ~0.67 V for *m*-$NaVO_3$ electrode are observed in the first cathodic sweep, which can be assigned to the intercalation reaction of Li^+ and the formation of SEI.

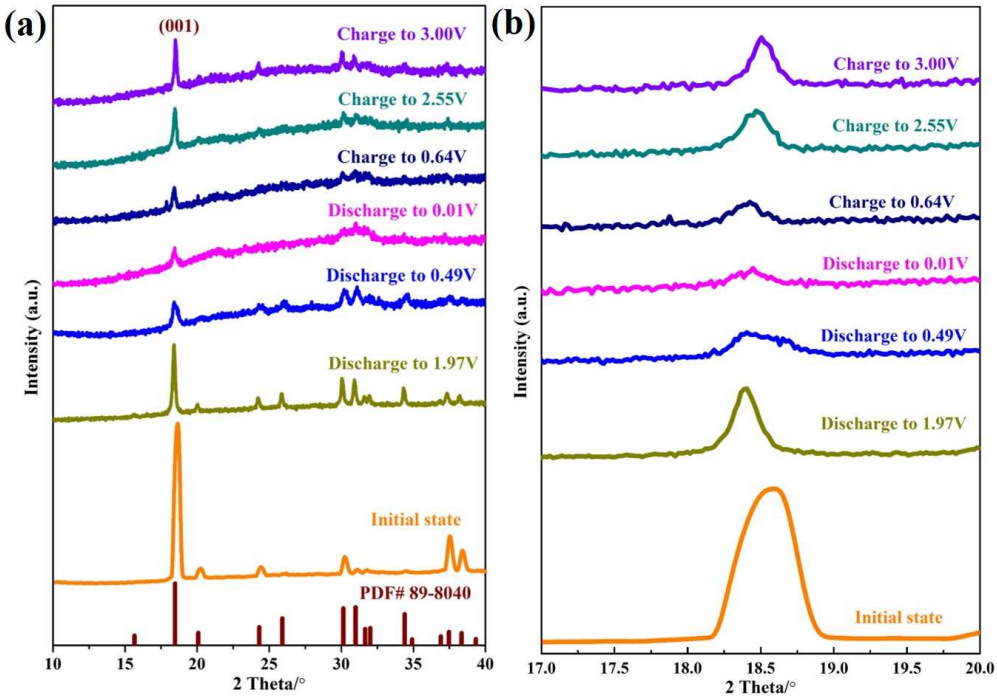

Figure S8. (a) *Ex-situ* XRD patterns and (b) corresponding Enlarged (001) peaks of *o*-NaV_2O_5 electrode after discharging and charging to different potential states at 100 mA g^{-1}.

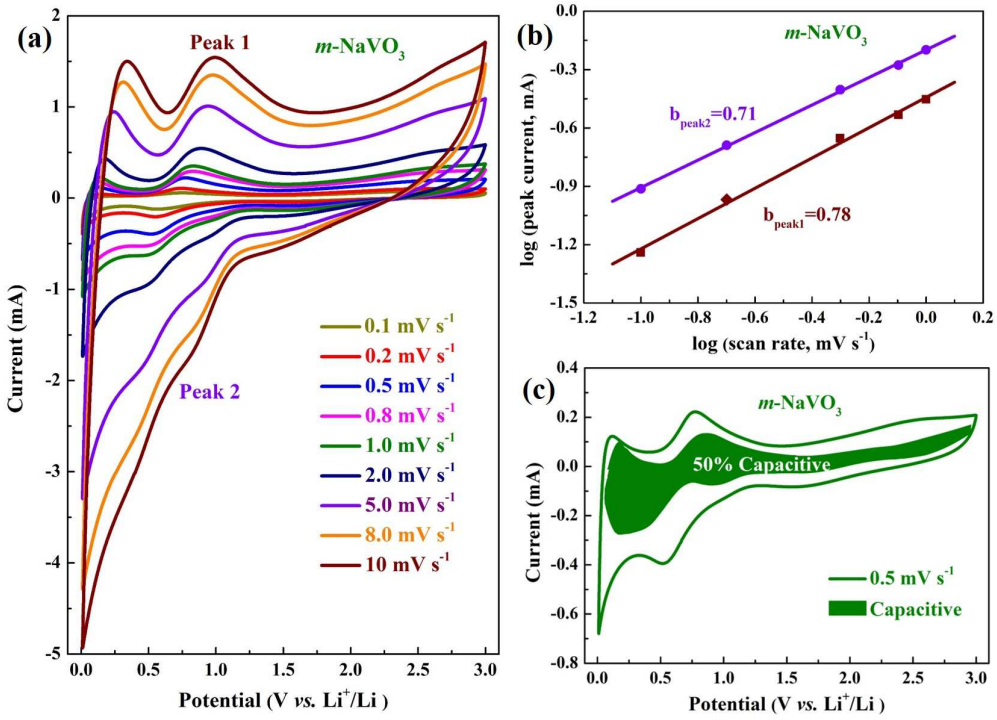

Figure S9. (a) CV curves at different scan rates from 0.1 to 10 mVs^{-1} within a potential range of 0.01 to 3.00 V (*vs*. Li^+/Li), (b) The fitted lines and log (peak current) *vs*. log (scan rate) plots at different oxidation and reduction states, and (c) The capacitive contribution shown by the shaded region at 0.5 mV s^{-1} for *m*-$NaVO_3$ electrode.

$$\log(i) = b\log(\upsilon) + \log(a) \quad \text{(S2)}$$

$$i(\mathrm{V}) = k_1\upsilon + k_2\upsilon^{1/2} \quad \text{(S3)}$$

where a and b are adjustable parameters, i is the current (mA) and υ is the scan rate (mVs^{-1}). The b-value is determined by the slop of $\log(i)$ - $\log(\upsilon)$ plots. When b-value approaches to 0.5, the system is mainly controlled by a diffusion process, while b-value is closed to 1.0, the system is mainly controlled by a capacitive process [3-4]. The total current response (i) at a fixed potential (V) can be divided into two parts including capacitive $k_1\upsilon$ and diffusion-controlled $k_2\upsilon^{1/2}$ [5-7]. The capacitive $k_1\upsilon$ is composed of the faradaic contribution from the charge-transfer process occurring on the surface/subsurface of electrode materials, referred to as pseudocapacitance; and the nonfaradaic contribution from double layer capacitive effect.

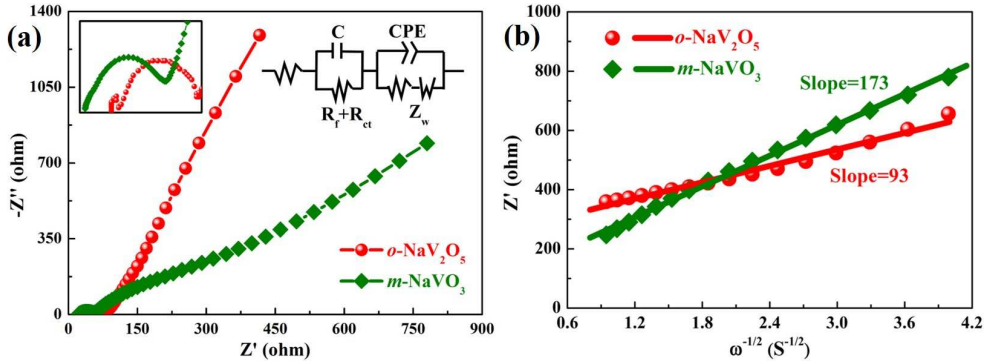

Figure S10. (a) Nyquist plots and (b) corresponding to linear fits in low frequency regions after 100 cycles at 200 mA g^{-1} for *o*-NaV_2O_5 and *m*-$NaVO_3$ electrode.

Before the measurements, all the samples are charged to 3.0 V at 200 mA g^{-1} after 100 cycles. The Nyquist plots in Figure S10(a) depict two incomplete semicircles at high-medium frequency and an inclined line at low frequency, which correspond to film resistance (R_f), charge transfer resistance (R_{ct}) and diffusion resistance (Z_w), respectively. Z_w is obtained by calculating the slope of the fitted line in Z'-$\omega^{-1/2}$ ($\omega=2\pi f$) curve in the low frequency region (Figure S10(b)). The total charge transfer resistance within all the interfaces is defined as $R_f + R_{ct}$. As shown in Figure S10(a), the total charge transfer resistance ($R_f + R_{ct}$) within all the interfaces of *o*-NaV_2O_5 electrode is 32 Ω, while that of *m*-$NaVO_3$ electrode is 36 Ω, suggesting the faster charge mobility. Meanwhile, the diffusion resistance of *o*-NaV_2O_5 electrode (97 $\Omega \cdot S^{1/2}$) is also much lower than that of *m*-$NaVO_3$ electrode (173 $\Omega \cdot S^{1/2}$), indicating the improved Li^+ diffusion (Figure S10(b)). Besides, the more-vertical line of *o*-NaV_2O_5 electrode (76° *vs*. 47°) at low frequency reveals its more remarkable capacitive-like behavior (Figure S10(a)). These results further demonstrate that the unique 3D assembled structure and orthorhombic structure of *o*-NaV_2O_5 improve its electrochemical reaction kinetic and then increases its pseudocapacitive contribution.

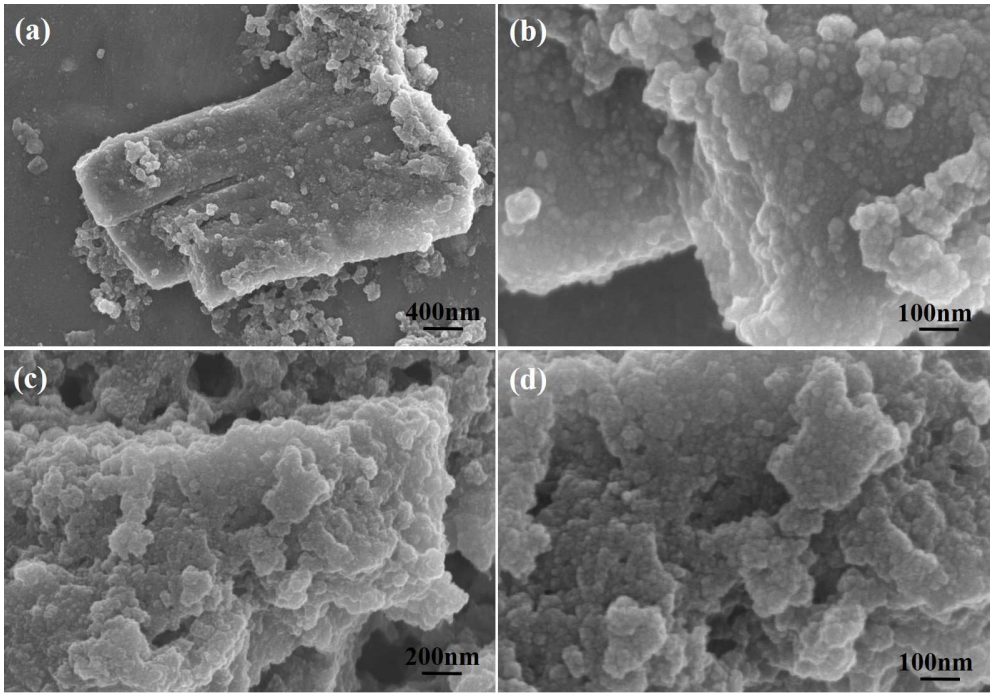

Figure S11. SEM images of NaV_2O_5 after (a and b) 100 and (c and d) 400 cycles at 200 mA h g^{-1}.

As shown in Figure S11, although the submicrobelts show the pulverization to a certain degree, the whole submicrobelts assembled microbundle-like morphologies of NaV_2O_5 are well retained, demonstrating its excellent structure stability during cycling.

References

1. Luo, Q.; Ma, H.; Hou, Q.; Li, Y.; Ren, J.; Dai, X.; Yao, Z.; Zhou, Y.; Xiang, L.; Du, H.; He, H.; Wang, N.; Jiang, K.; Lin, H.; Zhang, H.; Guo, Z., All-Carbon-Electrode-Based Endurable Flexible Perovskite Solar Cells. *Adv. Funct. Mater.* **2018,** *28* (11), 1706777, DOI: 10.1002/adfm.201706777.

2. Feng, Y.; Ge, S.; Li, J.; Li, S.; Zhang, H.; Chen, Y.; Guo, Z., Synthesis of 3,4,5-trihydroxy-2-[(hydroxyimino) methyl] benzoic acid as a novel rust converter. *Green Chem. Lett. Rev.* **2017,** *10* (4), 455-461, DOI: 10.1080/17518253.2017.1400590.

3. Hu, Z.; Zhu, Z.; Cheng, F.; Zhang, K.; Wang, J.; Chen, C.; Chen, J., Pyrite FeS_2 for High-rate and Long-life Rechargeable Sodium Batteries. *Energy Environ. Sci.* **2015,** *8* (4), 1309-1316, DOI: 10.1039/c4ee03759f.

4. Ran, F.; XiaobinYang; Shao, L., Recent progress in carbon-based nanoarchitectures for advanced supercapacitors. *Adv. Compos. Hybrid. Mater.* **2018,** *1* (1), 32-55, DOI: 10.1007/s42114-017-0021-2.

5. Wang, J.; Polleux, J.; Lim, J.; Dunn, B., Pseudocapacitive Contributions to Electrochemical Energy Storage in TiO_2 (Anatase) Nanoparticles. *J. phys. chem. c* **2007,** *111* (40), 14925-14931, DOI: 10.1021/jp074464w.

6. Simon, P.; Gogotsi, Y.; Dunn, B., Materials science. Where do batteries end and supercapacitors begin? *Science* **2014,** *343* (6176), 1210-1211, DOI: 10.1126/science.1249625.

7. Dong, J.; Jiang, Y.; Li, Q.; Wei, Q.; Yang, W.; Tan, S.; Xu, X.; An, Q.; Mai, L.,

Pseudocapacitive Titanium Oxynitride Mesoporous Nanowires with Iso-Oriented Nanocrystals for Ultrahigh-Rate Sodium-Ion Hybrid Capacitors. *J. Mater. Chem. A* **2017,** *22* (5), 10827-10835, DOI: 10.1039/c7ta00463j.